Geophysical Journal International

Geophys. J. Int. (2009) **179,** 1645–1657 doi: 10.1111/j.1365-246X.2009.04359.x

Finite frequency effects on global *S* diffracted traveltimes

Akiko To[1] and Barbara Romanowicz[2]

[1] *IFREE, JAMSTEC,* 3173-25 *Syowamachi Kanazawaku Yokohama* 236-0001, *Japan. E-mail: ato@jamstec.go.jp*
[2] *UC Berkeley Seismological Laboratory,* 215 *McCone Hall Berkeley* CA 94720-4760, *USA*

Accepted 2009 August 11. Received 2009 August 3; in original form 2009 April 30

SUMMARY

Many seismic observations have shown that strong heterogeneities exist in the bottom few hundreds kilometres of the mantle. Among different seismic phases, this region, that is, the D″ layer, can be most globally sampled by diffracted waves along the core mantle boundary. Here, we assess the amplitude and distribution of *S*-wave velocity variations in the D″ layer of an existing tomographic model. We compare observed SHdiff traveltime anomalies to synthetic ones obtained using (1) the coupled spectral element method (CSEM), which is our reference exact method, (2) non-linear asymptotic coupling theory (NACT) and (3) 1-D ray theory. Synthetic waveforms are calculated down to 0.057 Hz with a corner frequency at 0.026 Hz. In the first part of this paper, we compare the traveltime anomaly predictions from the three different methods. The anomalies from CSEM and NACT are obtained by taking cross-correlations of the 3-D and 1-D synthetic waveforms. Both NACT and standard ray theory, which are used in other recent tomographic models, suffer from biases in traveltime predictions for vertically varying structure near the core–mantle boundary: NACT suffers from saturation of traveltimes, due to the portion in the kernel calculation that is based on the reference 1-D model, while ray theory suffers from wave front healing effects in the vertical plane, exacerbated in the presence of thin low velocity layers. In the second part, we compare observed traveltime anomalies and predictions from CSEM. The data consists of 506 Sdiff traveltime anomalies from 15 events, obtained form global seismograph network records. The tomographic model does a good job at predicting traveltimes of Sdiff phases especially when the path mostly samples fast *S* velocity regions at the base of the mantle, such as beneath India, China, North America and Northern Pacific. The underprediction of the positive observed traveltime anomalies seems to occur in regions where the paths sample close to the border of the large low shear velocity provinces, such as beneath Southern Pacific, South of Australia, Philippine Sea plate and Northwestern Pacific Ocean. Inspection of the observed seismograms at higher frequencies indicate that (1) the gradient of structure is underestimated and (2) there are post-cursors to the Sdiff which bias the lower frequency traveltime measurements, and which are not taken into account by the tomographic inversion, because of the approximate theoretical framework.

Key words: Body waves; Wave scattering and diffraction; Wave propagation.

1 INTRODUCTION

In the last 10 yr, the modelling of various seismic phases, sensitive to structure at the base of the mantle, has shown that the D″ region is strongly heterogeneous, indicating the likely presence of both thermal and compositional variations (e.g. Lay *et al.* 1998; Wen *et al.* 2001; Garnero & McNamara 2008).

Two types of seismic waves are typically used to study this region: waves reflected at or near the core–mantle boundary (CMB) and diffracted waves. Recent analysis of seismic waves reflected at the CMB as well as their precursors have shown the presence of heterogeneous stratification in the D″ layer (e.g. Thomas *et al.* 2004; Chambers & Woodhouse 2006; Hutko *et al.* 2008). Detailed structures of laterally varying heterogenities are also investigated using reflected waves (ScS) combined with direct *S* waves, for densely sampled regions, such as the western Pacific (He *et al.* 2006; He & Wen 2009). However, given the poor distribution of favourable sources and receivers, only small areas of D″ can be sampled using reflected waves. The D″ region is most widely and globally sampled by diffracted waves, Sdiff or Pdiff, which typically travel along the CMB over more than 30 degrees of epicentral distance. Using these phases is essential for mapping the 3-D structure in the D″ layer. In particular, horizontal velocity jumps of 3–4.5 per cent have been reported in the D″ layer at the border of the two large-scale low

velocity provinces (LLVP), often also called 'superplumes', in the south Pacific and under Africa, based primarily on the analysis of Sdiff phases (e.g. Wen 2001; Ni *et al.* 2005; To *et al.* 2005). In To *et al.* (2005), we have shown the presence of relatively high frequency (less than 20s) post-cursors to Sdiff, for paths entering the African and Pacific superplume at grazing incidence with respect to the gradient of structure, which could be modelled by saturating the amplitude of the velocity anomalies across the fast to slow transition on the border of the African superplume, resulting in off-path wave propagation effects (multipathing) in the horizontal plane.

In order to map strong seismic velocity anomalies in D″ using waveforms of diffracted waves, appropriate tools are required. Ray theory, which is most commonly used in tomographic inversions of traveltimes, theoretically breaks down for diffracted waves. On the other hand, methods based on normal mode perturbation theory are suitable for diffracted waves, however, as they are largely based on first order approximations, they are theoretically limited to weak anomalies. Recently, numerical methods that can handle non-linear effects in wave propagation have been developed and applied to the case of waves diffracted on the CMB. In order to speed up computations, these methods are generally hybrid, connecting a region (D″) in which the wavefield is computed numerically, to the rest of the mantle, where the wavefield is computed using more standard approximate methods, either ray theory (e.g. Wen 2002; Ni *et al.* 2005) or normal modes in a spherical shell (Capdeville *et al.* 2003; To *et al.* 2005).

This paper consists of two parts. In the first part, we compare traveltimes of Sdiff waves computed using three different methods. The first method is 1-D ray theory, which is an expedient way to estimate traveltime anomalies, but is based on a high frequency approximation. It assumes that the waves are only sensitive to the structure along the infinitesimal ray path, and the sensitivity is uniform along the ray. It also assumes that the anomalies are small in amplitude, so that the ray is not bent due to 3-D heterogeneities. Ray tracing is conducted in a spherically symmetric (1-D) reference model PREM (Dziewonski & Anderson 1981).

The second method is non-linear asymptotic coupling theory (NACT; Li & Romanowicz 1995; Li & Romanowicz 1996) and is based on normal mode perturbation theory. In NACT, the effects due to lateral heterogeneities are composed of two parts. The first part, which is non-linear, takes into account the horizontally averaged structure along the great circle between the source and the station, and corresponds to the standard 'path average' (PAVA) approximation used in many tomographic inversions (e.g. Woodhouse & Dziewonski 1984; Nolet 1990). This corresponds to the inclusion of coupling effects due to lateral heterogeneity along a given mode dispersion branch (e.g. Romanowicz 1987). In the second part, coupling across mode branches is added in an asymptotic approximation to single scattering. This term is necessary in order to bring out the ray character of the sensitivity of body waves to structure. The NACT is a finite frequency, 2-D approximation, in the vertical plane containing the source and the receiver. For body waves, sensitivity outside of the ray path is considered only in the vertical plane.

The third method is the coupled spectral element method (CSEM), and will be our reference 'exact' method. It couples a spectral element computation in the heterogeneous target region (here D″) to a 1-D normal mode computation in the rest of the earth. The method is described in Capdeville *et al.* (2003).

By comparing *S* diffracted traveltime predictions using these three methods in a 3-D model as well as in simple models of radial velocity variations near the CMB, we discuss and compare the limitations of the two approximate methods in handling structural variations in the vertical plane, and point to some interesting features in the 3-D model.

The 3-D model considered here is based on the *S* velocity tomographic model SAW24B16 (Mégnin & Romanowicz 2000), a degree 24 'SH' model obtained by inversion of hand-picked transverse component body, surface and higher-mode waveforms, including SHdiff, by using NACT both for the forward and the inverse problems. We consider the 3-D structure of SAW24B16 in the bottom 370 km of the mantle, with 1-D PREM in the rest of the mantle. The 3-D velocity anomaly fades out gradually from 300 to 370 km above the CMB, so the 3-D model in the D″ layer is 'sandwiched' between the 1-D PREM model in the core and in the rest of the mantle. We refer to this model as SAW24B16**D**.

In the second part of the paper, we consider the limitations of linearization and of neglecting off-plane effects, and show where these are apparent near the core mantle boundary, by comparing observed Sdiff traveltime anomalies, to those predicted from SAW24B16**D** using CSEM.

2 RESOLUTION OF VERTICAL STRUCTURE NEAR THE CORE MANTLE BOUNDARY

2.1 Comparisons of traveltime predictions using different theoretical approaches

In order to measure the traveltime anomalies from NACT and CSEM synthetic waveforms for the 3-D model, synthetic waveforms from the 1-D model (PREM) are first created for each trace, using mode summation. The predicted traveltime anomalies are obtained by taking the cross correlations between PREM and the 3-D synthetics. CSEM synthetic waveforms are calculated up to 0.057 Hz with a corner frequency at 0.026 Hz. 800 Sdiff transverse component waveforms from 15 events are used for the comparison. The locations of events and stations are shown in Fig. 1.

Fig. 2(a) shows the comparison of traveltime anomalies predicted by CSEM and NACT. For anomalies smaller than 3–4 s, NACT does fine. However, traveltime anomalies predicted by NACT saturate around −6 s for negative anomalies and around 4 s for positive anomalies. This shows the limitations of the NACT in handling strong heterogeneities. It should be noted that the tomographic model provides anomalies of smaller amplitude compared to the real earth (Bréger & Romanowicz 1998; To *et al.* 2005). The effect due to the linearized term could be larger when the method is applied to observed data than when it is applied to the tomographic model.

Fig. 2(b) shows the comparison of traveltime anomalies predicted by CSEM and 1-D ray theory. For the 1-D ray calculation, the *Vs* anomalies at a depth of 2850 km in the original model (SAW24B16**D**) are assigned between 2850 km and the CMB(2891km). This is discussed further in Section 2.2. Fig. 2(b) indicates that CSEM gives smaller traveltime residuals if they are positive, whereas negative traveltime residuals are distributed along the $y = x$ line. One of the causes of the deviation from the $y = x$ line is the finite frequency effect (i.e. wave front healing, Nolet 1987; Hung *et al.* 2001), since it is included in CSEM but not in ray theory. Therefore, traveltime corrections made based on the bold black line of Fig. 2(b) are called 'finite frequency corrections' hereafter. This result indicates that waveforms are affected differently depending on whether positive or negative velocity anomalies are

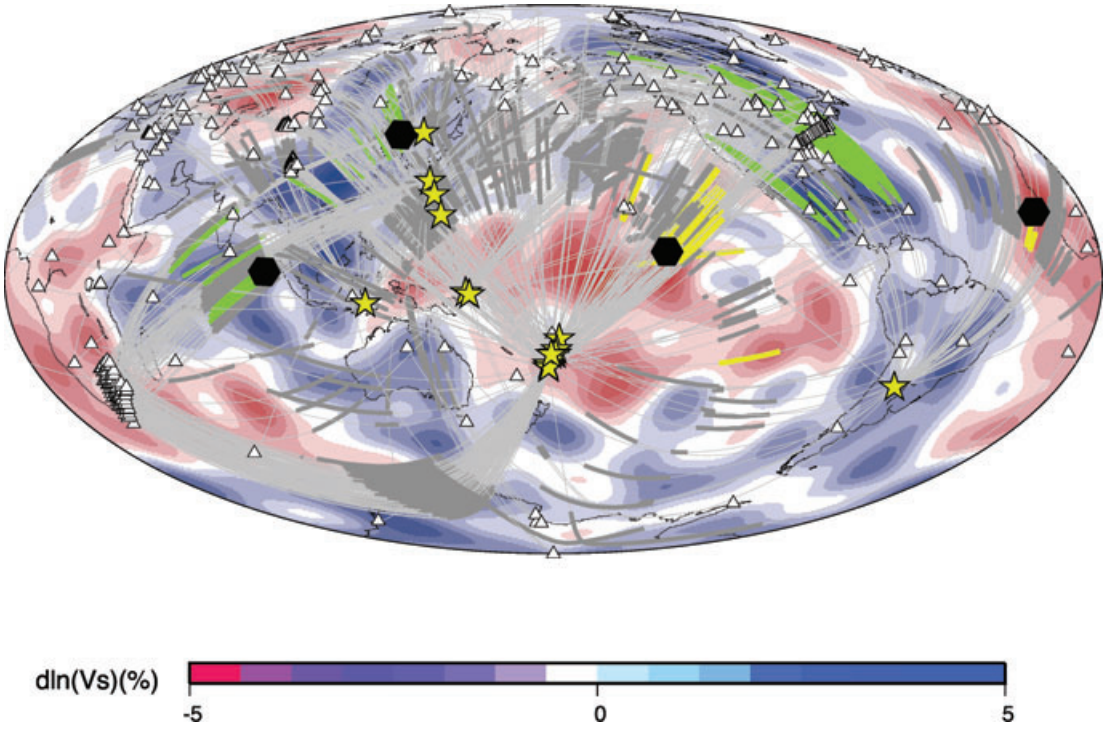

Figure 1. Distribution of paths used in the comparison of traveltimes computed using three different methods. Stations are shown by triangles. Events are shown by yellow stars. The background model is SAW24B16 at a depth of 2850 km. The diffracting portions of Sdiff along the CMB are shown by thick lines. The paths are shown in yellow if the predicted traveltime anomalies by SEM are larger than 2 s and those from ray theory are larger than 7 s. The paths are shown in green if predicted traveltime anomalies by SEM are less than −6 s and those from ray theory are also less than −6 s. Black hexagons show the locations for which the *Vs* anomaly profiles are shown in Fig. 4.

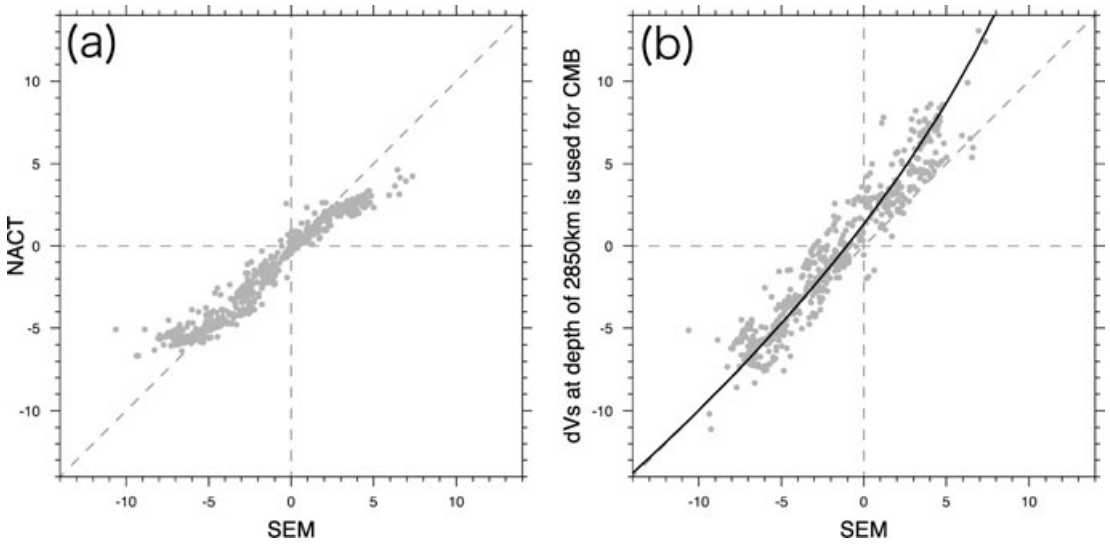

Figure 2. Comparison of traveltime anomaly predictions using three different methods. The traveltime anomalies are calculated for 800 Sdiff phases. The model has the 3-D *Vs* structure of SAW24B16 in a 370- km-thick layer at the bottom of the mantle. (a) Comparison between CSEM and NACT. (b) Comparison between 1-D ray theory and CSEM. The dashed line is a third-order polynomial function which fits the data best in a least-squares sense.

sampled near the CMB. The cause of this asymmetry is examined in the next section.

2.2 Cause of the asymmetric behaviour between positive and negative traveltime anomalies

We examine the cause of this asymmetry and determine whether it is due to the particular 3-D structure used or whether it is present for any kind of structure. First, we compare the traveltime predictions using CSEM and ray theory for eight different 1-D models. The models and results are shown in Fig. 3. The models are created based on PREM with modifications to the *S* velocity structure in the D″ layer. The eight models are defined by combinations of three factors, the depth extent of the velocity anomaly (100 or 300 km), the amplitude of the anomaly (2 or 4 per cent) and the sign of the anomaly (positive or negative). Fig. 3 shows that the two

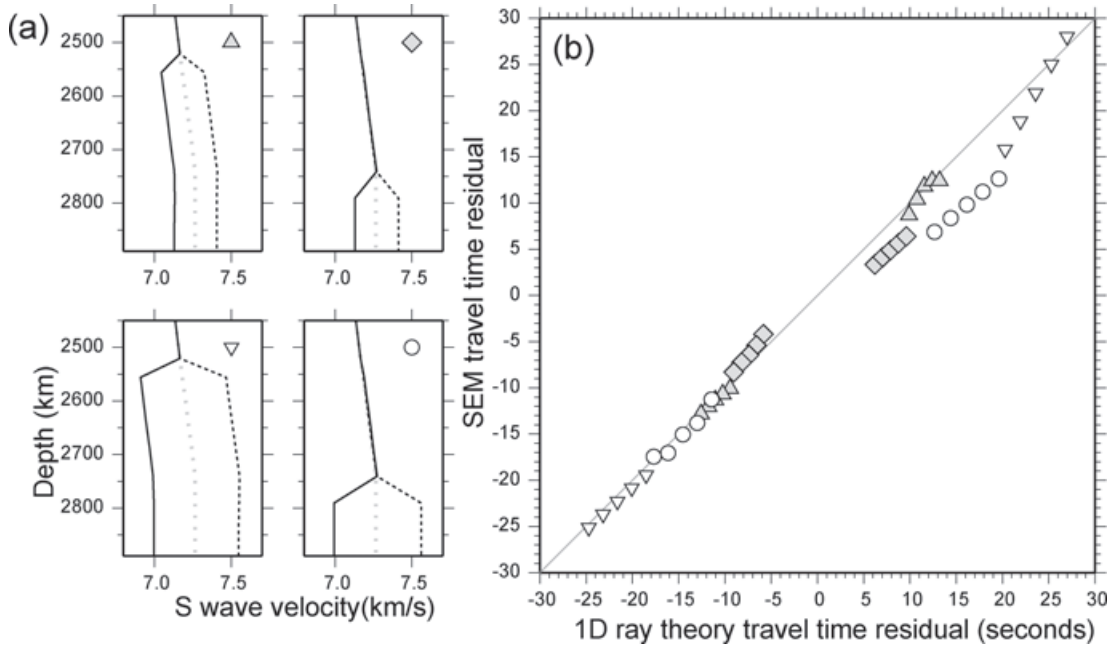

Figure 3. (a) Profiles of eight different 1-D models which are used in the comparison of traveltime predictions. Thick grey dotted lines correspond to the PREM profile. Solid and dashed lines show the profiles for negative and positive velocity anomaly models, respectively. The profiles shown in the top left-hand panel (grey triangles) have 2 per cent velocity anomaly in the bottom 300 km of the mantle. The top right-hand panel (grey diamond) shows profiles with 2 per cent anomalies in the bottom 100 km of the mantle. The bottom left-hand panel (inverted triangle) shows the profiles with 4 per cent anomalies in the bottom 300 km of the mantle. The bottom right-hand panel (open circle) shows profiles with 4 per cent anomalies in the bottom 100 km of the mantle. (b) A comparison of predicted traveltime residuals for Sdiff between 1-D ray theory and SEM for the 1-D models shown in (a), indicated by corresponding symbols. The results are shown at five different source–receiver distances for each model(105°, 110°, 115°, 120° and 125°).

methods give similar residuals when the slow anomaly layer is thick (300 km) or when there is a fast velocity layer at the base of the mantle, regardless of the thickness of the layer. On the other hand, the traveltime residuals from the CSEM computation are smaller than those from 1-D ray theory, when a thin (100 km) slow velocity layer is present at the bottom of the mantle. The effect in the case of a slow velocity anomaly is stronger when the velocity contrast is stronger. This result illustrates that the 'broad-band' Sdiff waves are sensitive to the vertical velocity gradient near the CMB: when it is negative (slow velocity anomaly), there is an averaging effect over a certain thickness above the CMB, resulting in a smaller positive traveltime anomaly. This effect is described as an SH interface wave in other papers (e.g. Okal & Geller 1979; Wen 2002) which emerges with the existence of a low velocity zone at the base of the mantle. When the gradient is positive (fast velocity anomaly), there is no such effect, and the width of the sensitivity of the wave is confined to the fast velocity regions.

Second, we examine whether the 3-D model has such thin slow anomaly layers that cause the asymmetry shown in Fig. 3. Profiles of the model for four selected locations are shown in Fig. 4. The locations are shown by black hexagons in Fig. 1. They are located in regions which are sampled by paths with one of the two following features: (1) predicted traveltime anomalies by CSEM are larger than 2 s and the predictions from ray theory are larger than 7 s. They correspond to paths which deviate from the $y = x$ line with large positive traveltime anomalies in Fig. 2. In Fig. 1(top), the diffracting portion of the paths of these data are shown by yellow lines. (2) Predicted traveltime anomalies by CSEM are less than -6 s and the predictions from the ray theory are also less than -6 s. They correspond to the data which are distributed around $y = x$ line in Fig. 2 with large negative traveltime anomalies. The diffracting portions of these paths are shown by green lines in Fig. 1. The bottom panels of Fig. 4 show the existence of slow velocity regions at the bottom of the mantle. The right-hand top panel shows that fast velocity regions also exist, whereas the left-hand top panel shows the presence of a fast velocity region where velocity does not change much in the bottom 200 km of the mantle.

Moreover, we examined the existence of a thin slow velocity layer at the bottom of the mantle by comparing the amplitude of *Vs* anomalies at different depths in model SAW24B16. This is done by comparing ray theoretical traveltime anomalies for the same traces as Fig. 2 calculated for different velocities assigned to the diffracted portion of the ray path. On the *y*-axis of Fig. 5 (left-hand panel) are the traveltime anomalies calculated for a model, which has the *Vs* anomaly at 2800 km of the original model assigned between a depth of 2800 km and the CMB (2891 km). The rest of the model is the same as SAW24B16**D**. The value of *x*-axis for grey dots in Fig. 5 (left-hand panel) are traveltime anomalies from the original model, where the actual CMB anomaly is used at CMB. The values of *x*-axis for black dots are calculated from a model which uses the *Vs* anomalies at a depth of 2850 km from 2850 km down to CMB. These values are the same as the ones shown in the *x*-axis of Fig. 2(a). The deviation of the plot (Fig. 5) from $y = x$ line becomes larger as the anomalies of deeper depths are used in the ray tracing. It suggests that the *Vs* anomalies get significantly slower at deeper depths below the depth of 2800 km, at least in the regions sampled by the traces with large positive traveltime anomalies.

Fig. 5(right-hand panel) shows the comparison of traveltime predictions between CSEM and 1-D ray theory. Grey solid circles show exactly the same plot as Fig. 2(b), where the ray tracings are done

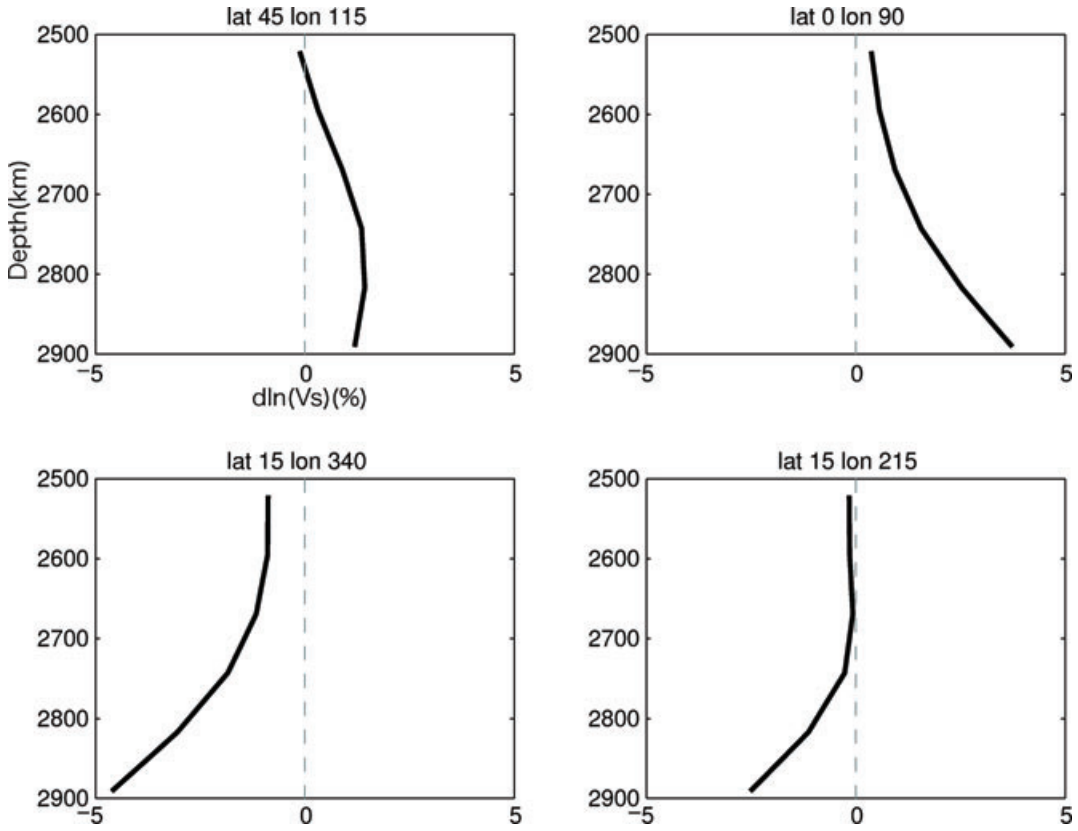

Figure 4. *S* velocity anomaly profiles of SAW24B16 in the D″ layer for four locations shown by black hexagons in Fig. 1. The latitudes and longitudes of the locations are shown in each panel.

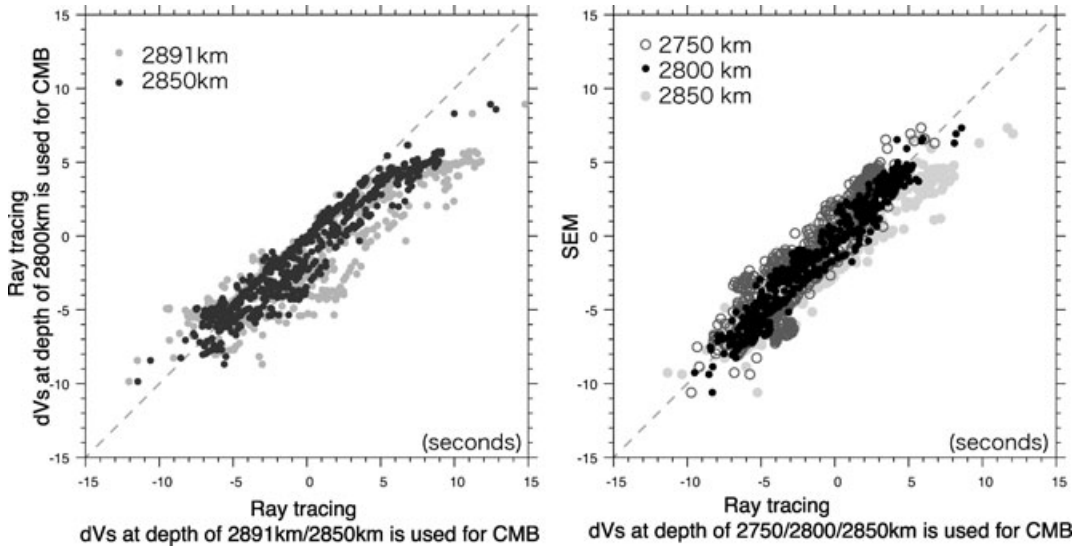

Figure 5. Left-hand panel: comparison of traveltime predictions for three different models using 1-D ray theory. Values on the *y*-axis are obtained from a model which has the *Vs* structure of SAW24B16 at the depth of 2800 km assigned to the depth range 2800 km CMB (2891 km). SAW24B16D is used for the rest of the mantle. Values on the *x*-axis for black dots are obtained for a model which has the structure of SAW24B16 at the depth of 2850 km assigned to the depth range 2850–2891 km. Values on the *x*-axis for grey dots are obtained from the original SAW24B16 where the actual *Vs* anomalies at the CMB are used. Right-hand column: comparison of traveltime predictions from CSEM and ray theory. *Y*-axis shows traveltime anomalies obtained by CSEM for SAW24B16**D**. Values on *x*-axis are obtained by ray theory. They are obtained for models which have *Vs* anomalies at depths of 2750/2800/2850 km assigned from those depths down to CMB.

by using the anomalies at depth of 2850 km of the original model as the anomalies in the depth range of 2850 and 2891 km (CMB). Black solid circles and grey open circles correspond to the case, respectively, where the anomaly at the depth of 2800/2750 km is used between the depth of 2800/2750 km and CMB for the ray tracing. This figure shows that the traveltime anomalies predicted by CSEM have best correlation with traveltime anomalies obtained by using *Vs* anomalies at 2800 km in the ray tracing.

The results of the experiments (Figs 3 and 5) suggest that the asymmetry in the traveltime comparison (Fig. 2b) is due the wave front healing effect which is intensified by the existence of slow velocity layer in the 3-D model. The model has a strong negative vertical gradient of *Vs* anomaly amplitudes in some slow velocity regions, with a thin slow velocity layer just above CMB. Because of such a thin slow anomaly layer on the CMB, diffracted waves become more sensitive to the structure somewhat above the CMB which results in smaller positive traveltime anomalies for Sdiff, than predicted by ray theory. On the other hand, the model does not show strong vertical *Vs* anomaly gradients for the fast velocity regions sampled by this data set in the D″ layer (Fig. 5). Besides, when a fast velocity layer is present at the bottom of the mantle, waveforms are mainly sensitive to the amplitudes of the fast anomaly and are not so sensitive to the vertical structure or gradient of the *Vs* structure. It is therefore not clear whether such negative gradients can be detected with the analysis of broadband Sdiff phases. Because the model has slow velocity anomalies in a thin layer at the bottom of the mantle and because of the finite frequency effect, the traveltime comparison between CSEM and 1-D ray theory shows asymmetry between positive and negative anomalies.

3 LATERAL VARIATIONS OF STRUCTURE NEAR THE CMB: COMPARISON OF OBSERVED AND PREDICTED TRAVELTIME ANOMALIES

We compared predicted traveltime anomalies obtained using CSEM for model SAW24B16**D** with observed traveltime anomalies (Fig. 6). The number of data is 506 and there are fewer paths than shown in Fig. 1(a), since noisy observed waveforms are removed. The observed traveltime anomalies, shown on the *x*-axis in Fig. 6, are obtained by cross-correlating observed waveforms with PREM synthetic waveforms created by normal mode summation. A band-pass filter, which has corner frequencies at 0.01 and 0.026 (Hz), is applied to observed waveforms, so that the frequency components become consistent with CSEM synthetics. Cutoff frequencies of the filter are 0.001 and 0.057 (Hz). The predicted traveltime anomalies, shown on the *y*-axis of Fig. 6, are obtained by taking the cross correlations between PREM and the 3-D synthetics created by CSEM for model SAW24B16**D**. The predicted traveltime shifts due to the 3-D structure of the rest of the mantle, namely from 370 km above CMB to the surface, (hereafter referred to as overlying mantle correction) are obtained by 1-D ray theory from SAW24B16. In Fig. 6(a), all the corrections, namely the overlying mantle correction, station altitude correction and ellipticity correction (Kennett & Gudmundsson 1996), are subtracted from the observations, in order to show the comparison of observed and predicted traveltime anomalies due to the D″ layer structure alone. On the other hand, in Fig. 6(b), the corrections are added to the predictions from CSEM, to show the comparison of the traveltime anomalies accumulated along the entire path. The comparison is given in two different ways in order to show the size of the misfit with respect to the range of the predicted traveltime anomalies due to the D″ layer structure (Fig. 6a) and the range of observed anomalies (Fig. 6b). The misfit between observed and predicted traveltimes from the 3-D model is called 'residual' hereafter, in order to distinguish it from 'predicted anomaly', which indicates the difference in the predicted traveltimes between 3-D and 1-D (PREM) models. The residual is obtained as the difference between *x*- and *y*-axis values of each data point in the figure. Data are plotted in different colours depending on the size of observed traveltime anomalies (the difference between observed and 1-D(PREM) synthetic traveltimes) and the residual (the difference between the observed and 3-D (SAW24B16) predicted traveltimes). Most data are distributed roughly along $y = x$ line in Fig. 6, which

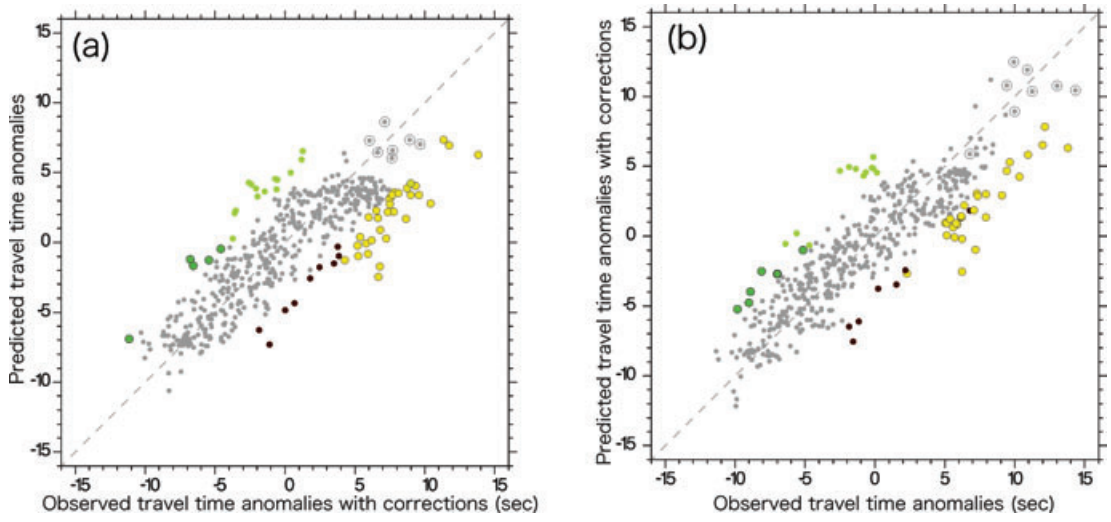

Figure 6. Comparison of observed and predicted (3-D) traveltime anomalies with respect to PREM. The predicted (3-D) traveltimes anomalies are obtained from SAW24B16 by CSEM for the 3-D structure of the D″ layer and by 1-D ray theory for the rest of the mantle. Data are plotted in different colours depending on the size of observed traveltime anomalies [the difference between observed and predicted (1-D) traveltimes. Hereafter referred to as *observed anom.*] and residuals (the difference between the observed and predicted (3-D) traveltimes, which corresponds to the differences of the values of *x*- and *y*-axis in the figure. Hereafter referred to as *res.*). The path distribution of the data is shown in Fig. 8. Grey dots: $-4 <= res. <= 4$ s, Grey dots surrounded by a circle: $-4 <= res. <= 4$ and *predicted anom.* > 5 and *observed anom.* > 5, Yellow dots: $4 < res.$ and $4 <$ *observed anom.*, Green dots: $res. < -4$ and *observed anom.* < -4, Light green dots: $4 < res.$ and *observed anom.* > -4, Brown dots: $res. < -4$ and *anom.* < 4 (a) The overlying mantle correction, station altitude correction and ellipticity correction are subtracted from the observation. (b) The corrections are added to the predictions from CSEM. Data are coloured depending on observed anomalies with corrections as shown in *x*-axis of panel (a), therefore in panel (b) they do not show clear separation of distribution depending on colours.

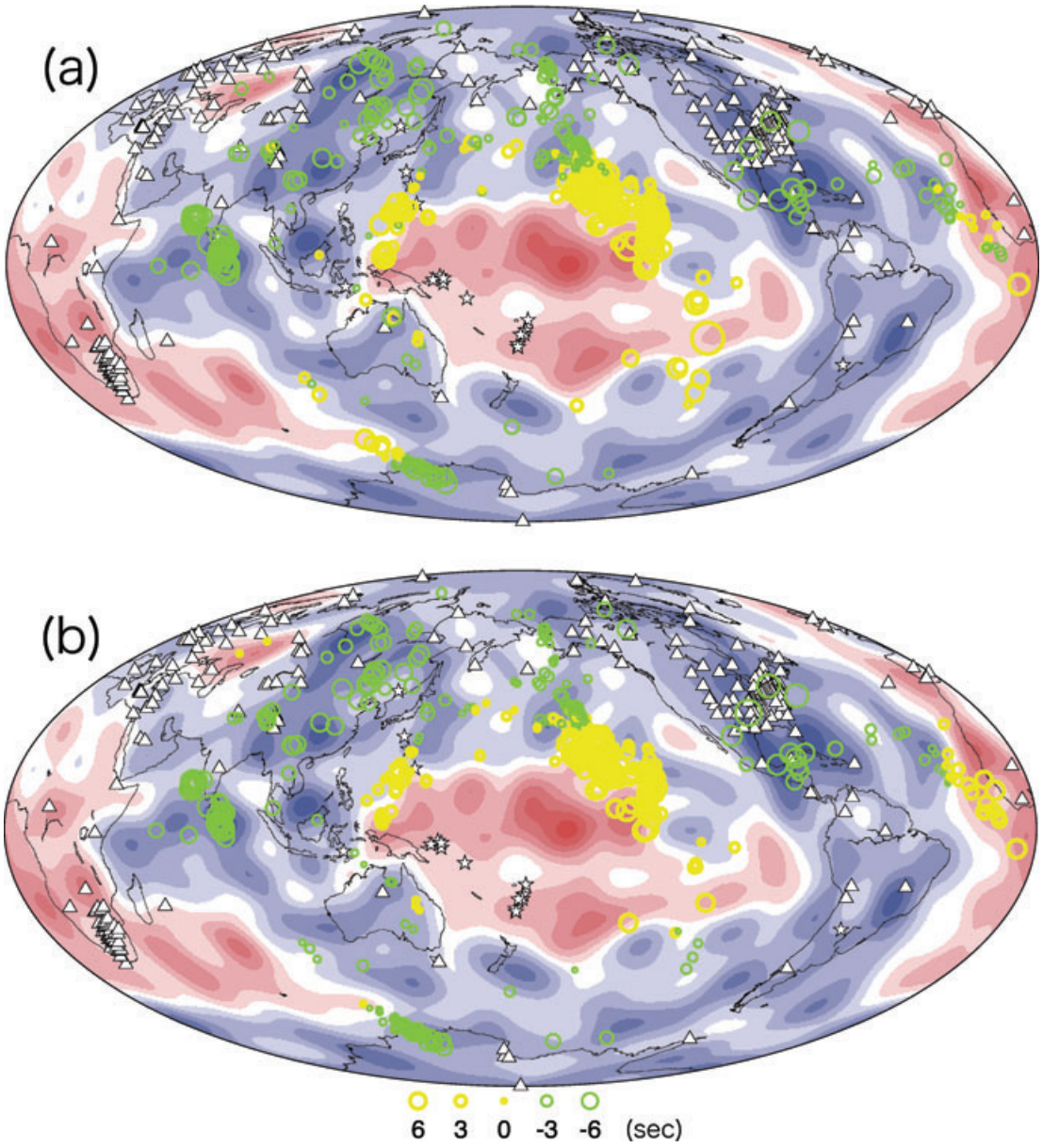

Figure 7. (a) Distribution of observed traveltime anomalies. The anomalies are plotted at the midpoint of diffracting portions of Sdiff paths. The overlying mantle corrections, station altitude corrections and ellipticity corrections are subtracted from the measurements. (b) Distribution of predicted traveltime anomalies due to the D″ layer structure. The anomalies are obtained by CSEM.

indicates that model SAW24B16 gives good traveltime predictions overall. 89 per cent of the measurements have a traveltime residual of less than 4 s. 82 per cent of the measurements have traveltime residual of less than 3 s. Data with predicted residuals that are less than 4 s are shown by grey dots. We consider that residuals of 4 s or less may be caused by other effects than the imperfection of the 3-D model considered. The residuals should be caused not only by the difference between the given 3-D model and actual earth mantle structure, but also by errors due to measurements, noise, source time functions and others. By separating the data this way, Fig. 6 clearly shows that there are more underpredicted data than over-predicted ones. All the data, which have residuals larger than 4 s and for which the size of observed anomalies is larger than 4 s, seem to be underpredicted (i.e. The size of observed traveltime anomalies is larger than that of predicted traveltime anomalies) If the criterion is set to 3 s, we start to see some overpredicted data. The figure also shows that there are more underpredicted data of positive observed traveltime anomalies, which are shown by yellow dots, than those of negative anomalies, which are shown by green dots.

Fig. 7 shows the spatial distribution of observed (top panel) and predicted (bottom panel) traveltime anomalies. Corrections for overlying mantle structure, ellipticity and station altitude are subtracted from the observed traveltime anomalies. They are plotted at the midpoints of the diffracting portions of the Sdiff paths. Fig. 8 shows the distribution of traveltime residuals. The colours of the paths are chosen depending on the size of the residuals and anomalies of each trace. The colours are consistent with the colours used in Fig. 6. Diffracting portions of Sdiff paths for all the data are plotted in Fig. 8(a). In Figs 8(b) and (c), the paths of well predicted data (residuals $< =4$ s) and poorly predicted data (residuals >4 s) are plotted, respectively.

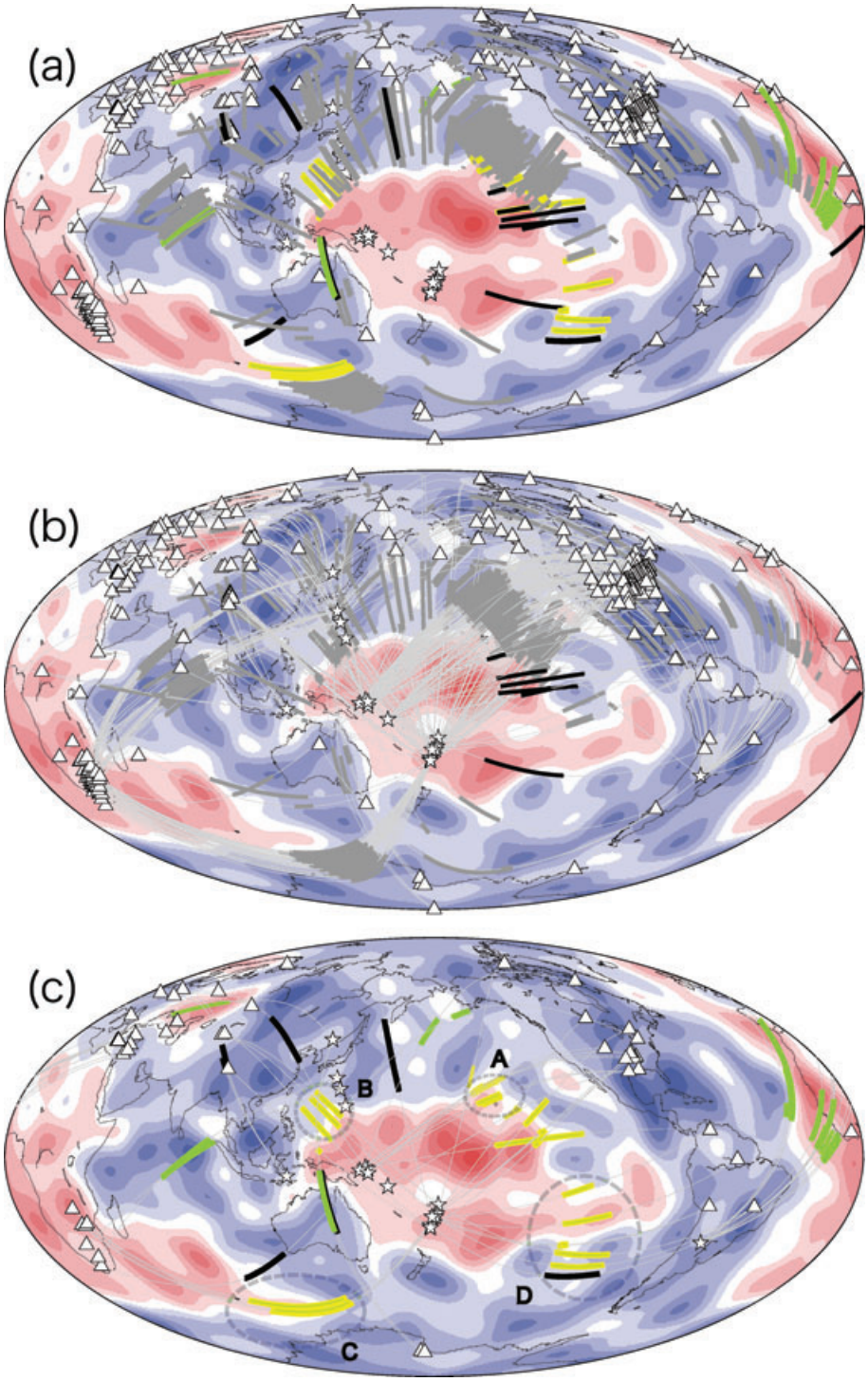

Figure 8. Diffracting portions of the Sdiff paths used in the comparison between observed and synthetic traveltimes. The colours of the paths depend on the size of traveltime difference between observations and predictions from 1-D (PREM) and 3-D (SAW24B16) models. They correspond to the colours of data plotted in Fig. 6. Paths shown by black thick lines correspond to the data shown by grey dots surrounded by circles in Fig. 6. (a) all data. (b) Paths for which observed traveltimes are well predicted using SAW24B16. The traveltime difference between observations and predictions (3-D) is less than 4 s. (c) Paths for which the traveltime difference between observations and predictions (3-D) is larger than 4 s.

Figs 7 and 8 indicate that traveltimes are predicted well in the regions with fast *S*-wave velocity at the base of the mantle, such as beneath India, China, North America, Northern Pacific and the southern side of the African Superplume. The underprediction of positive observed traveltime residuals seems to occur in regions where the paths sample close to the border of the two superplumes, such as beneath southern Pacific, south of Australia, Philippine Sea plate and northwestern Pacific Ocean. In this data set, there are only a few paths which only sample slow regions of the D″ layer and whose observed and predicted traveltime anomalies are positive

and large (black lines in Fig. 8 and grey dots surrounded by a circle in Fig. 6). Most traces with positive anomalies sample the border of the superplumes where the *S*-velocity changes from negative to positive. Therefore, it is difficult to assess whether slow velocity anomalies in the model are properly estimated or underestimated in general. In the following paragraphs, we look into causes of the underprediction of the positive traveltime anomalies of the regions encircled by grey dashed lines in Fig. 8(c).

3.1 Northeastern Pacific

The large traveltime anomalies of paths in the northeastern Pacific Ocean (Fig. 8c, region A) are caused by a contamination from an Sdiff post-cursor which drags the Sdiff phase backward when a low pass filter is applied. Fig. 9 shows the distribution of traveltime anomalies obtained from four events located in Papua New Guinea. Fig. 9(c) indicates that traveltimes are significantly underpredicted

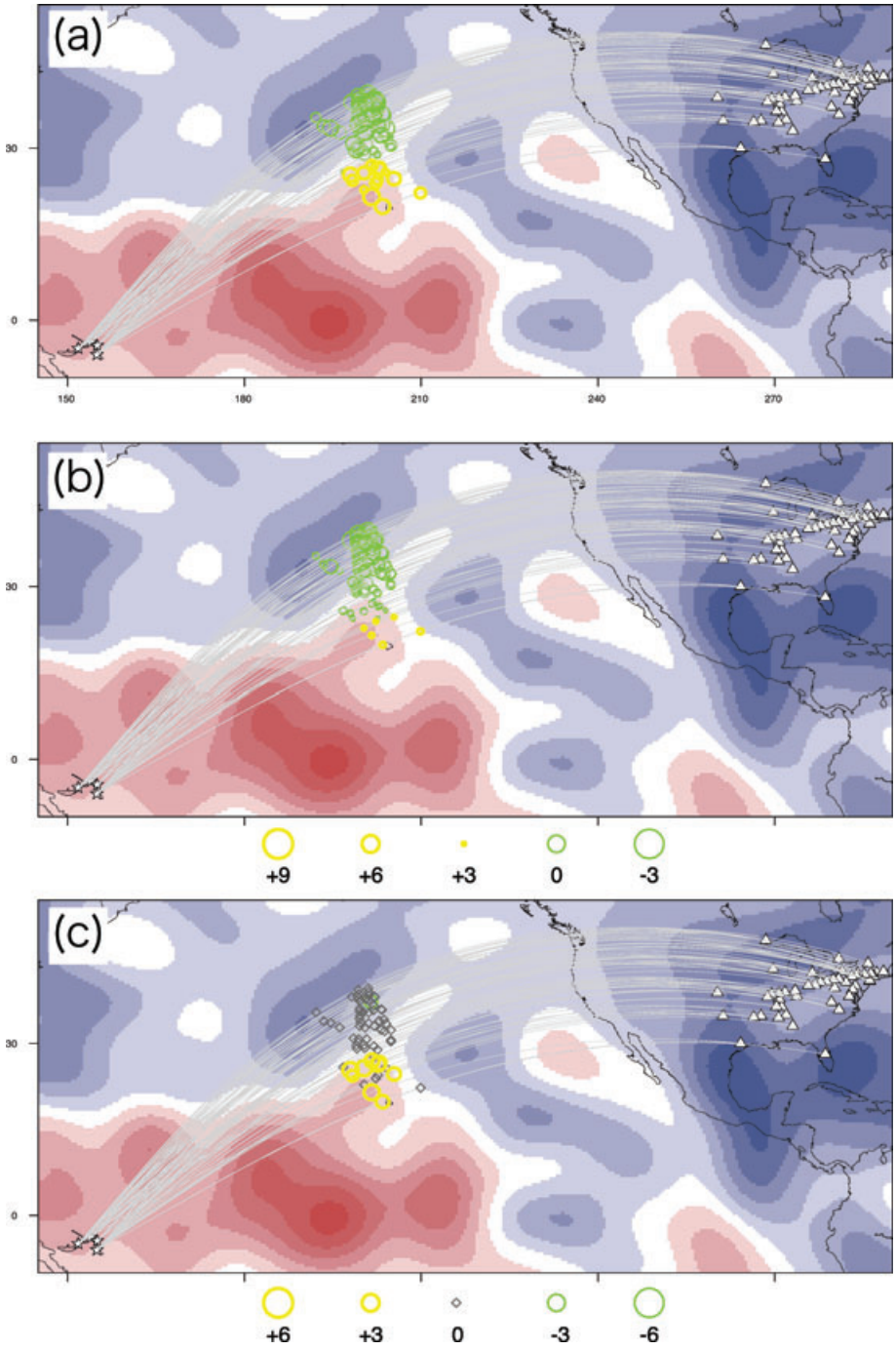

Figure 9. Distribution of traveltime anomalies and residuals for the traces which sample the northeastern Pacific. Note that colour scales of traveltime anomalies are different from Fig. 7. (a) Distribution of observed traveltime anomalies. (b) Distribution of predicted traveltime anomalies obtained from SAW24B16 by using CSEM for D″ layer and 1-D ray theory for the 3-D structure of the rest of the mantle. (c) Traveltime residuals, which are the differences between observed and predicted anomalies. Grey squares are plotted for the traces whose residuals are less than 3 s.

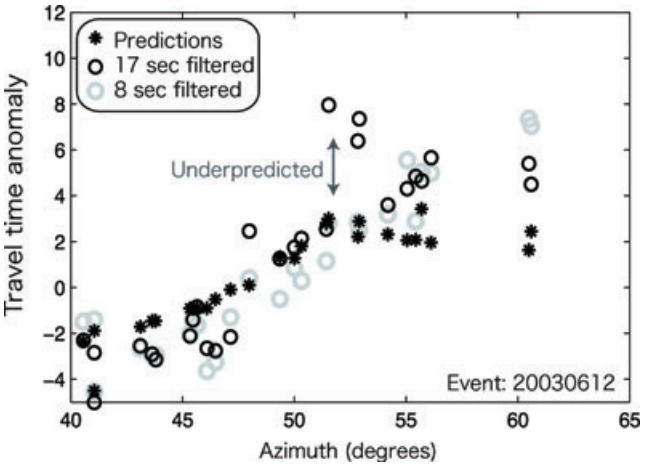

Figure 10. Traveltime anomalies with respect to azimuth for one of the events shown in Fig. 7 whose waveforms are shown in Fig. 11. Predictions are obtained by CSEM calculated down to 0.057 Hz for the D″ layer and by 1-D ray theory for the rest of the mantle. The two sets of observed anomalies are obtained by cross correlating PREM synthetics and observed waveforms in the two different frequency ranges.

for paths with large azimuths, which are more southerly, and graze the trend of the heterogeneity. In Fig. 10, we plot traveltime anomaly variations with respect to azimuth for one of the four events. Measurements made in two different frequency ranges are compared. The first one is done by applying a bandpass filter, which has corner frequencies at 0.01 and 0.026 (Hz), to the observed and PREM synthetic waveforms (hereafter referred to as low frequency measurements). These are the same measurements as those shown in Figs 6, 7 and 9. The other is done by applying a bandpass filter which has corner frequencies at 0.01 at 0.125 (Hz) to the waveforms (referred to as high frequency measurements hereafter). The two measurements are consistent at small azimuths, but become inconsistent at azimuths around 48°. At azimuths around 52°, the low frequency measurements are large and they are substantially underpredicted, while high frequency measurements are consistent with the predictions. The waveforms of the data are plotted in Fig. 11 and they are aligned in order of azimuth. High frequency waveforms (Fig. 11, right-hand panel) show that the Sdiff phase is followed by large post-cursors which are not seen in PREM synthetic waveforms. In the high frequency waveforms, the pulses of the main phase and post-cursor are clearly separated (Fig. 11 right-hand panel), while in the low frequency waveforms, they merge and become one large pulse (Fig. 11 left-hand panel). The post-cursor starts to appear from azimuth around 48°, which is consistent with the azimuth where the discrepancy between the measurements of the two frequency ranges starts to appear in Fig. 10. The large traveltime anomalies of the low frequency measurements are caused by contamination by post-cursors. The observation leads to the following two points. (1) The emergence of the anomalous post-cursors indicates the presence of a structure with abrupt change in *S* velocity. It is necessary to use broad-band waveforms, up to at least 0.125 (Hz), in order to

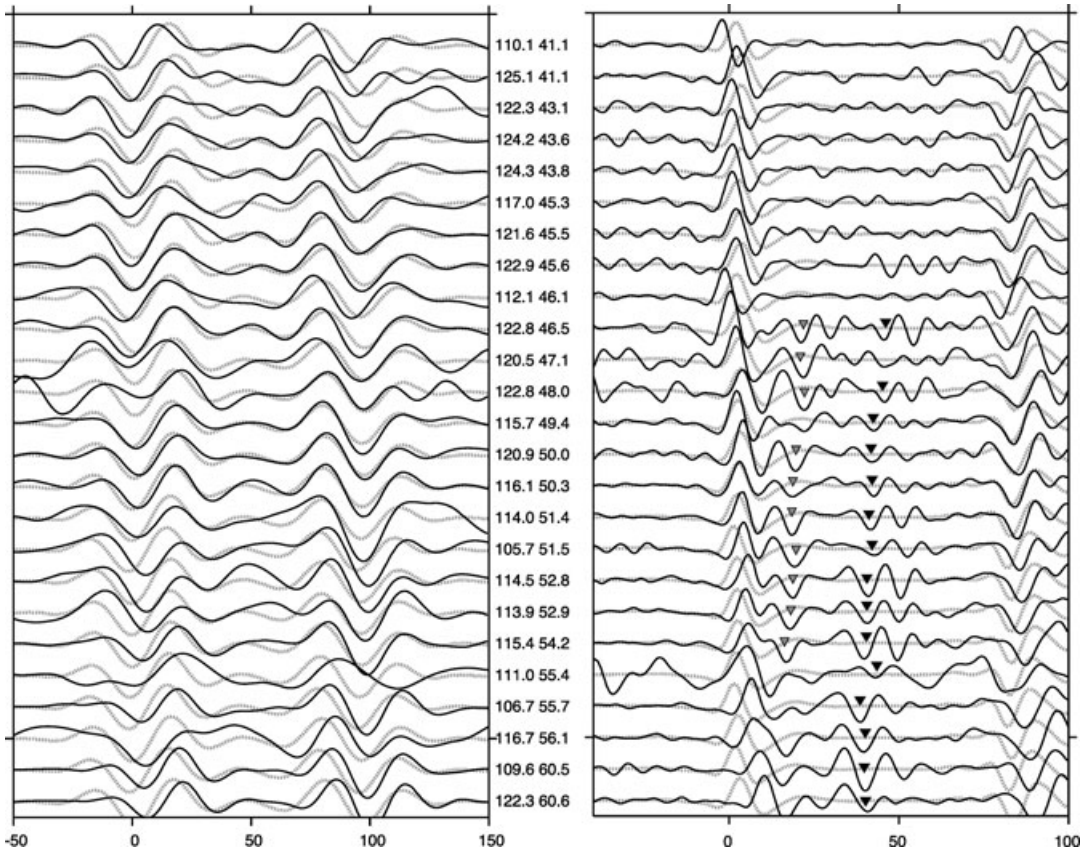

Figure 11. Observed transverse component velocity waveforms for an event in Papua New Guinea with depth of 185 km (date: 2003 June 12, M_w 6.2) recorded at stations in United States, also shown in To and Fukao (2007). Traces are aligned in order of azimuth. Waveforms are filtered in two different ways. Black lines show observed waveforms, grey dotted lines show PREM synthetics. The distance and backazimuth of each trace are indicated between the two panels. Left-hand panel: transverse component bandpass filtered with corner frequencies at 0.01 and 0.026 Hz. Right-hand panel: bandpass filtered with corner frequencies at 0.01 and 0.125 Hz.

constrain the details of the structure, such as its geometry and gradient at the boundary. (2) The alignment of the post-cursor with respect to azimuth suggests that the structure is likely located outside of the vertical plane containing the great circle path between the source and the station. NACT does not take into account the structure outside the great circle plane, therefore such a structure cannot be resolved in the inversion or results in a bias in the inversion process. This would be the case for any 2-D calculation in the vertical great circle plane (e.g. Wen 2002). The importance of the 2-D structure on fitting broadband Sdiff waveforms has been intensively discussed (e.g. Wen 2002). Our observation shows that effect of 3-D structure is not negligible. The underestimation of the traveltime anomalies is therefore caused by an abrupt structure, possibly located outside of the great circle plane, which is not resolved in the inversion and does not appear in the model.

3.2 Northwestern Pacific

The underprediction of traveltimes for paths which sample the northwestern Pacific (Fig. 8c, region B) shows strong station location dependence. Fig. 12 shows that large traveltime residuals are observed for traces recorded in two stations KN.AML and IU.AAL in Kazakhstan. The cause of the traveltime delay is on the station side rather than source side of Fiji, although the depth at which the slow velocity anomaly is located is unknown.

3.3 Southern Pacific

The traveltime underprediction of paths which sample the southern Pacific (region D in Fig. 8c) is caused by low resolution of the tomographic model in this region. Fig. 13 shows that the traveltime anomaly in Sdiff increases with respect to station backazimuth. Observed traveltime anomalies of SKS and SKKS phases are plotted as well, but they do not show the sharp increase with respect to backazimuth. The cause of the rapid shift of Sdiff anomalies is therefore likely in the D″ layer, since SKKS and Sdiff have very similar paths in the upper mantle. On the other hand, the predicted Sdiff traveltime anomalies do not show the increase with respect to backazimuth. Also there is no such structure in the D″ layer of SAW24B16, which is slower on the northern side and faster on the southern side. In the region, which is sampled by the paths shown in Fig. 13(a), *Vs* changes primarily from east to west and not from north to south. Therefore, the cause of the underpredictions of traveltimes is the low resolution of the model in the D″ layer, due to paucity of data sampling this south Pacific region.

3.4 Indian Ocean

Region D in Fig. 8(c) was studied previously (Wen 2001; Ni *et al.* 2005; To *et al.* 2005). The Sdiff waveforms show the presence of post-cursors for paths subparallel to the fast-to-slow velocity transition at the border of the African plume. These post-cursors could be reproduced using CSEM with a model in which the velocity anomalies were saturated (To *et al.* 2005).

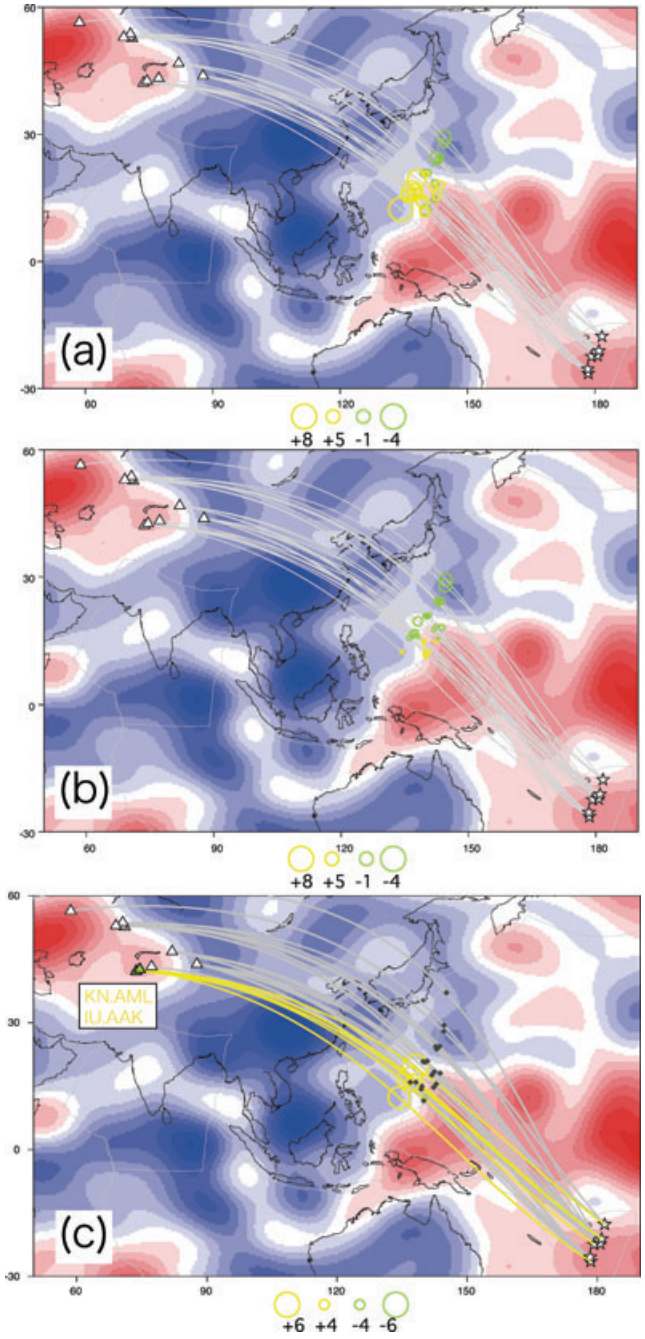

Figure 12. Distribution of traveltime anomalies and residuals for traces which sample the northwestern Pacific. Note that the colour scale for traveltime anomalies is different from Fig. 7. (a) Distribution of observed traveltime anomalies. (b) Distribution of predicted traveltime anomaleis obtained from SAW24B16 by using CSEM for the D″ layer and 1-D ray theory for the structure of the rest of the mantle. (c) traveltime residuals, which are the differences between the observed and predicted anomalies. Grey squares indicate traces whose residuals are smaller than 3 s. The paths are shown by yellow lines and circles for traces with residuals larger than 3 s.

4 DISCUSSION AND CONCLUSIONS

Both NACT and standard ray theory, which is used in other recent tomographic models, suffer from biases in traveltime predictions for vertically varying structure near the core–mantle boundary: NACT suffers from saturation of traveltimes, due to the portion in the kernel calculation that is based on the reference 1-D model, while ray theory suffers from a combination of wavefront healing effects in the vertical plane, exacerbated in the presence of thin low velocity layers. NACT-based inversions could be improved by computing the kernels in the average 3-D model corresponding to the portion of path sampling D″, while in ray theoretical treatments, caution

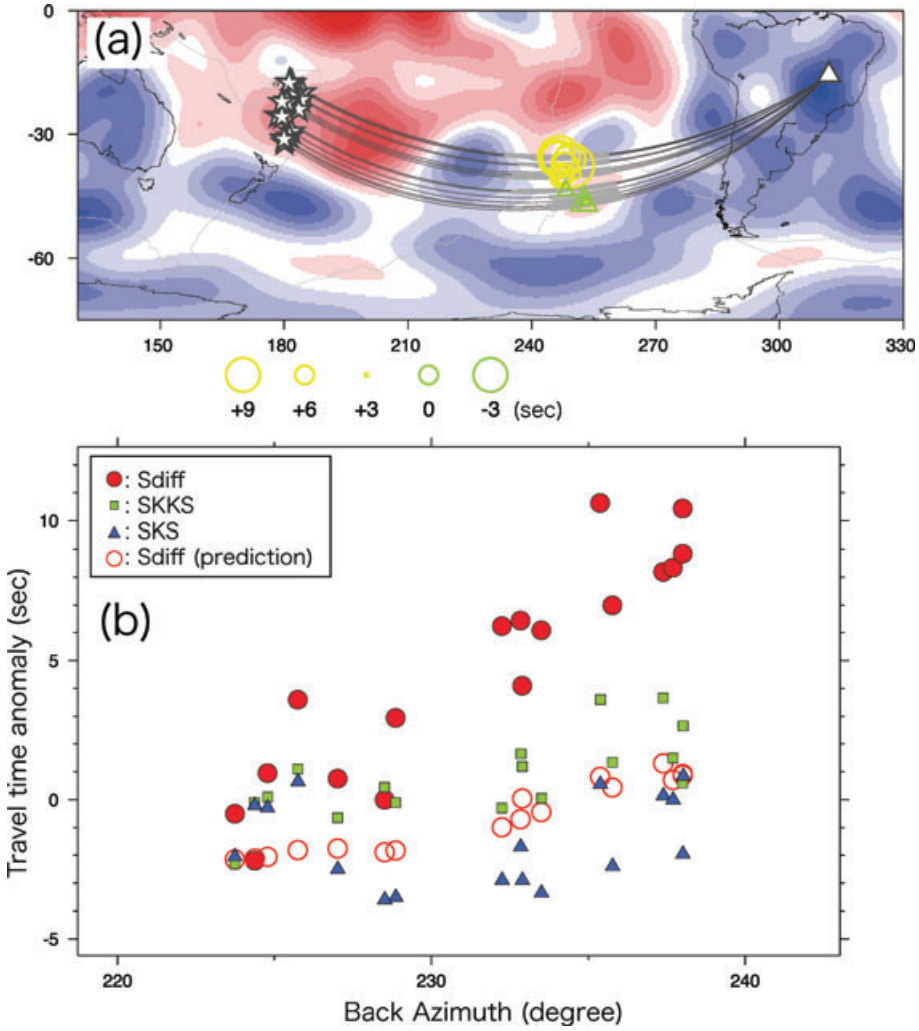

Figure 13. Results for region D in Fig. 8. Events are located in the Fiji-Tonga region. Some events are added to the events shown in Fig. 7. Their depths vary from 116 to 630 km. The station is BDFB in Brazil. (a) Map view of paths and corresponding Sdiff traveltime anomalies and (b) observed Sdiff, SKS and SKKS traveltime anomalies, plotted as a function of backazimuth, and predicted Sdiff anomalies for model SAW24B167D.

should be taken when choosing the velocity model in which the traveltimes are computed, near the CMB. From Fig. 4, it appears that in the construction of SAW24B16, distinct profiles with depth in low and high velocity regions could be distinguished, which is likely due to a combination of using NACT (rather than ray theory) as well as the inclusion of *S* and ScSn waveforms, in addition to Sdiff. There are regions with very low velocities at the base of the mantle, but none with correspondingly high velocity. Determining whether this has any geodynamic significance is however beyond the scope of this paper, because it is not clear whether this is due to limitations in the modelling approach used in the construction of SAW24B16, or a feature of the real earth.

This study has shown that, in general, model SAW24B16 does a good job at predicting traveltimes of Sdiff phases low pass filtered at 0.026 Hz: 89 per cent of the traveltime residuals, obtained by comparison with synthetics computed using CSEM in the 3-D model have an amplitude of less than 4 s. On the other hand, ∼10 per cent of the sampled paths show larger discrepancies with 3-D model predictions. Most of the affected paths correspond to transition regions between slow and fast velocities at the border of the two 'superplumes', and occur in regions where either sampling is poor (South Pacific), or where the paths are subparallel to the gradients of structure (e.g. North Pacific or Indian Ocean). In the latter case, inspection of the observed seismograms at higher frequencies indicate that (1) the gradient of structure is underestimated and (2) there are post-cursors to the Sdiff which bias the traveltime measurement, when it is performed at lower frequencies, and which also are not taken into account by the tomographic inversion, because of the approximate theoretical framework. Current tomographic models of the lower mantle rely on approximate theories which cannot handle strong lateral heterogeneity, through partial or complete linearization of the problem. NACT, which was used in the construction of model SAW24B16 tested here, only considers effects of heterogeneity in the vertical plane containing source and receiver, and cannot handle off plane 3-D effects, which also appear at higher frequency than is considered so far in NACT, but which provide significant constraints on lateral gradients of structure at the border of the LLVPs.

In the future, it is important to try and improve sampling of the D″ layer, especially under the southern oceans, but also to use theoretical approaches at the base of the mantle that can handle strong lateral heterogeneity, in the same way as progress is made in this direction in the case of the crust and upper mantle, through the use of the spectral element method (e.g. Tape *et al.* 2007; Lekic

& Romanowicz 2008). Waveform modeling at higher frequencies (down to 10 s) will also be helpful, although care must be taken to eliminate contamination from the upper mantle.

ACKNOWLEDGMENTS

We thank Jeannot Trampert and an anonymous reviewer for their reviews and helpful comments. We also thank IRIS data agency for the broadband data. Most figures were generated using the Generic Mapping Tools [P. Wessel and W.H.F. Smith, EOS Trans. AGU, 72, 441, (1991)]. This study was supported by a grant from NSF (EAR-0106000). Berkeley Seismological Laboratory Contribution #09-19.

REFERENCES

Bréger, L. & Romanowicz, B., 1998. Thermal and chemical 3-D heterogeneity in D″, *Science,* **282,** 718–720.

Capdeville, Y., To, A. & Romanowicz, B., 2003. Coupling spectral elements and modes in a spherical earth: an extension to the 'sandwich' case, *Geophys. J. Int.,* **154,** 44–57.

Chambers, K. & Woodhouse, J.H., 2006. Investigating the lowermost mantle using migrations of long-period, *Geophys. J. Int.,* **166,** 667–678.

Dziewonski, A.M. & Anderson, D.L., 1981. Preliminary reference earth model, *Phys. Earth planet. Inter.,* **25,** 297–356.

Garnero, E.J. & McNamara, A.K., 2008. Structure and dynamics of Earth's lower mantle, *Science,* **320,** 626–628.

Hung, S.-H., Dahlen, F.A. & Nolet, G., 2001. Wavefront healing: a banana-doughnut perspetive, *Geophys. J. Int.,* **146,** 289–312.

Hutko, A.R., Lay, T., Revenaugh, J. & Garnero, E.J., 2008. Anti-correlated seismic velocity anomalies from post-perovskite in the lowermost mantle, *Science,* **320,** 1070–1074.

Lay, T., Williams, Q. & Garnero, E.J., 1998. The core-mantle boundary layer and deep Earth dynamics, *Nature,* **392,** 461–468.

Lekic, V. & Romanowicz, B., 2008. Global Upper mantle radially anisotropic model developed using the spectral element method, *EOS, Trans. Am. geophys. Un.,* **89**(53), Fall Meet. Suppl., DI11A-04.

Li, X.D. & Romanowicz, B., 1995. Comparing of global waveform inversions with and without considering cross-branch modal coupling, *Geophys. J. Int.,* **121,** 695–709.

Li, X.D. & Romanowicz, B., 1996. Global mantle shear velocity model developed using nonlinear asymptotic coupling theory, *J. geophys. Res.,* **101,** 11 245–22 271.

He, Y., Wen, L. & Zheng, T., 2006. Geographic boundary and shear velocity structure of the 'Pacific anomaly' near the core-mantle boundary beneath western Pacific, *Earth planet. Sci. Lett.,* **244,** 302–314.

He, Y. & Wen, L., 2009. Structural features and shear-velocity structure of the 'Pacific Anomaly', *J. geophys. Res.,* **114,** B02309, doi:10.1029/2008JB005814.

Kennett, B.L.N. & Gudmundsson, O., 1996. Ellipticity corrections for seismic phases, *Geophys. J. Int.,* **127,** 40–48.

Ni, S., Helmberger, D.V. & Tromp, J., 2005. 3D Structure of the African super plume from waveform modeling, *Geophys. J. Int.,* **161,** 283–294.

Mégnin, C. & Romanowicz, B., 2000. The three-dimensional shear velocity structure of the mantle from the inversion of body, surface and higher-mode waveforms, *Geophys. J. Int.,* **143,** 709–728.

Nolet, G., 1987. *Seismic Tomography: With Applications in Global Seismology and Exploration Geophysics,* D. Reidel Publishing Co., Dordrecht, Holland.

Nolet, G., 1990. Partitioned wave-form inversion and 2-dimensional structure under the network of autonomously recording seismographs, *J. geophys. Res.,* **95,** 8499–8512.

Okal, E.A. & Geller, R.J., 1979. Shear-wave velocity at the base of the mantle from profiles of diffracted SH waves, *Bull. seism. Soc. Am.,* **69,** 1039–1053.

Romanowicz, B., 1987. Multiplet-multiplet coupling due to lateral heterogeneity: asymptotic effects on the amplitude and frequency of the earth's normal modes, *Geophys. J. R. astr. Soc.,* **90,** 75–100.

Tape, C., Liu, Q. & Tromp, J., 2007. Finite-frequency tomography using adjoint methods. Methodology and examples using membrane surface waves, *Geophys. J. Int.,* **168,** 1105–1129.

Thomas, C., Kendall, M.J. & Lowman, J., 2004. Lower mantle seismic discontinuities and the thermal morphology of subducted slabs, *Earth planet. Sci. Lett.,* **225,** 105–113.

To, A., Romanowicz, B., Capdeville, Y. & Takeuchi, N., 2005. 3D effects of sharp boundaries at the borders of the African and Pacific Superplumes: observation and modeling, *Earth planet. Sci. Lett.,* **233,** 137–153.

To, A., & Fukao. Y., 2007. Seismic velocity anomalies in the D″ layer beneath Hawaii, *EOS, Trans. Am. geophys. Un.,* **88**(52), Fall Meet. Suppl., Abstract S14A-03.

Wen, L., 2001. Seismic evidence for a rapidly varying compositional anomaly at the base of the Earth's mantle beneath the Indian Ocean, *Earth planet. Sci. Lett.,* **194,** 83–95.

Wen, L., Silver, P., James, D. & Kuehnel, R., 2001. Seismic evidence for a thermo-chemical boundary layer at the base of the Earth's mantle, *Earth planet. Sci. Lett.,* **189,** 141–153.

Wen, L., 2002. An SH hybrid method and shear velocity structures in the lowermost mantle beneath the central Pacific and South Atlantic oceans, *J. geophys. Res.,* **107,** doi:10.1029/2001JB000499.

Woodhouse, J.H. & Dziewonski, A.M., 1984. Mapping the upper mantle; three-dimensional modeling of Earth structure by inversion of seismic waveforms, *J. geophys. Res.,* **89,** 5953–5986.